Additive Manufacturing 43 (2021) 102004

Contents lists available at ScienceDirect

Additive Manufacturing

journal homepage: www.elsevier.com/locate/addma

Research Paper

Stability of crystallographic texture in laser powder bed fusion: Understanding the competition of crystal growth using a single crystalline seed

Takuya Ishimoto [a,b,1], Koji Hagihara [a,b,1], Kenta Hisamoto [a], Takayoshi Nakano [a,b,*]

[a] Division of Materials and Manufacturing Science, Graduate School of Engineering, Osaka University, 2-1, Yamadaoka, Suita, Osaka 565-0871, Japan
[b] Anisotropic Design & Additive Manufacturing Research Center, Osaka University, 2-1, Yamadaoka, Suita, Osaka 565-0871, Japan

ARTICLE INFO

Keywords:
Laser powder bed fusion
Crystallographic texture
Stability
Crystal growth
Single crystal

ABSTRACT

In metal additive manufacturing, crystallographic orientation control is a promising method for tailoring the functions of metallic parts. However, despite its importance in the fabrication of texture-controlled functional parts, the stability of the crystallographic texture is not widely discussed. Herein, the crystallographic texture stability under laser powder bed fusion was investigated. Two methodologies were employed. One is that a laser scanning strategy was alternately changed for a specific number of layers. The other is a "seeding" experiment in which single-crystalline substrates with controlled crystallographic orientations in the building (*z*-) direction and the *xy*-plane (perpendicular to the building direction) were used as the starting substrate. The transient zone width, where the crystallographic orientation was inherited from the layer beneath, was analyzed to evaluate the texture stability. The crystallographic direction of the seed within the *xy*-plane, rather than the building direction, determined the transient zone width, i.e., the texture stability. In particular, the texture in the newly deposited portion was stable when the laser scanning direction matched the <100> orientation in the underneath layer, otherwise the crystal orientation switched rapidly, such that the <100> orientation was parallel to the scanning direction. Interestingly, the crystallographic orientation along the building direction in the underneath layer hardly impacted the stability of the texture. Therefore, for the first time, it has been clarified that the <100> orientation in the scanning direction, rather than the building direction, was preferentially stabilized, whereas the orientation in the other directions secondary stabilized.

1. Introduction

In recent years, metal additive manufacturing (AM) has unleashed new possibilities for the fabrication of high value-added products and has attracted the most significant attention in various metal processing technologies. Generally, since AM is characterized by its flexible shaping ability, it has been utilized for the fabrication of a variety of products, including those with hollow structures, three-dimensional complex porous bodies, and custom-made products [1–4]. Moreover, in some cases, AM has been combined with topology optimization [5,6]. Further, in addition to controlling the shape of products, recent studies have revealed the promising potential of metal AM for controlling the crystallographic texture of metallic materials [7–14]. Crystallographic texture, which is independent of the shape of products, is an important factor contributing to the functionality of metallic materials, such as the mechanical properties. The most recent study demonstrated that laser powder bed fusion (LPBF), the most common powder bed fusion process in AM, facilitated the fabrication of products with diverse crystallographic textures, ranging from randomly crystallographically oriented polycrystalline to highly textured single-crystalline-like microstructures [7,14]. This was achieved by varying the balance between the thermal gradient at the solid/liquid interface, the migration velocity of the solid/liquid interface, and the melt pool shape [9,10].

Highly textured materials, including single-crystalline materials, are highly desired for specific applications requiring extremely superior mechanical properties because materials with preferential

* Corresponding author at: Division of Materials and Manufacturing Science, Graduate School of Engineering, Osaka University, 2-1, Yamadaoka, Suita, Osaka 565-0871, Japan.
E-mail address: nakano@mat.eng.osaka-u.ac.jp (T. Nakano).
[1] These authors contributed equally to this work.

https://doi.org/10.1016/j.addma.2021.102004
Received 29 January 2021; Received in revised form 5 April 2021; Accepted 9 April 2021
Available online 8 May 2021

crystallographic orientations feature mechanical anisotropies, such as Young's modulus [15,16], yield stress and elongation [17], fatigue resistance [18], and creep resistance [19]. Although there are several reports on the formation of a single-crystalline-like texture by LPBF, the formation mechanism has not been elucidated thus far. Our recent investigation revealed that a laser scanning strategy (SS), the combination of laser scanning patterns between layers, impacts the evolution of the crystallographic texture in a beta-type Ti–15Mo–5Zr–3Al alloy with a body-centered cubic (bcc) structure [14]. The SS_X in which the laser was only scanned bidirectionally along the *x*-axis (Fig. 1(a1)) evolves the texture in which <011> and <100> orient along the building (BD) and scanning directions, respectively (Fig. 1(a2)). However, the SS_X in which the laser was bidirectionally scanned with a rotation of 90° between the layers (Fig. 1(b1)) produces the texture in which <100> orients along the BD and duplicated scanning directions (Fig. 1(b2)). Herein, these two types of crystallographic textures are referred to as $\{011\}_z\langle 100\rangle_x$ and $\{001\}_z\langle 100\rangle_x$ textures, respectively. A similar texture evolution using LPBF was reported for the X-scan [9,12,20] and XY-scan [12,21,22] strategies using metallic materials with cubic crystal structures (bcc or face-centered cubic (fcc)).

The scanning strategy-dependent texture development was briefly discussed in a previous paper [14] that the feasibility of an epitaxial growth from the adjacent track and underneath layer is important. The preferential growth direction of the columnar cells for the fcc and bcc metals is parallel to <100> [23]. Therefore, the crystallographic texture is formed so that the consistency of <100> cell growth between adjacent tracks and between underneath layers is established, as shown in Fig. 1 (a3, b3). In such a way, in the SS_X, the cell elongation direction in the cross-section of the melt pool is finally fixed along the ±45° directions from the BD (Fig. 1(a3)). As a result, the identical orientation is achieved in the left and right regions in the melt pool. Conversely, in the SS_XY, the ±45° cell growth cannot be achieved owing to the rotation of the laser scanning direction by 90° between layers. If the <100>-oriented cell growth occur at ±45° direction from the BD in a layer under the SS_XY, <100> cannot grow in a continuous direction in the next layer. Therefore, the <100>-oriented cell grows at angles of 0° and 90° from the BD (Fig. 1(b3)) so that the melt pools generated by X-scan and the next Y-scan have a consistent crystallographic orientation, resulting in the evolution of the $\{001\}_z\langle 100\rangle_x$ texture. In this way, the importance of the crystal growth with a continuous crystallographic orientation between the tracks and between the layers, i.e., an epitaxial growth, was reported. However, little is understood about the initial stage of developing behavior of crystallographic orientation before the epitaxial growth is achieved.

In this study, we highlight the two above-mentioned types of crystallographic textures and investigate the stability of the crystal orientation by changing the scanning strategy between the layers. In addition, single-crystalline materials with varied and controlled crystallographic orientations are used as seeds to systematically investigate the stability of the crystallographic texture developed by LPBF. The beta-type Ti–15Mo–5Zr–3Al alloy authorized for use as a biomaterial by the International Organization for Standardization (ISO) (ISO 5832–14) is utilized because tailoring the mechanical properties via controlling the textures is a promising strategy for enabling functional improvement in medical metallic implants.

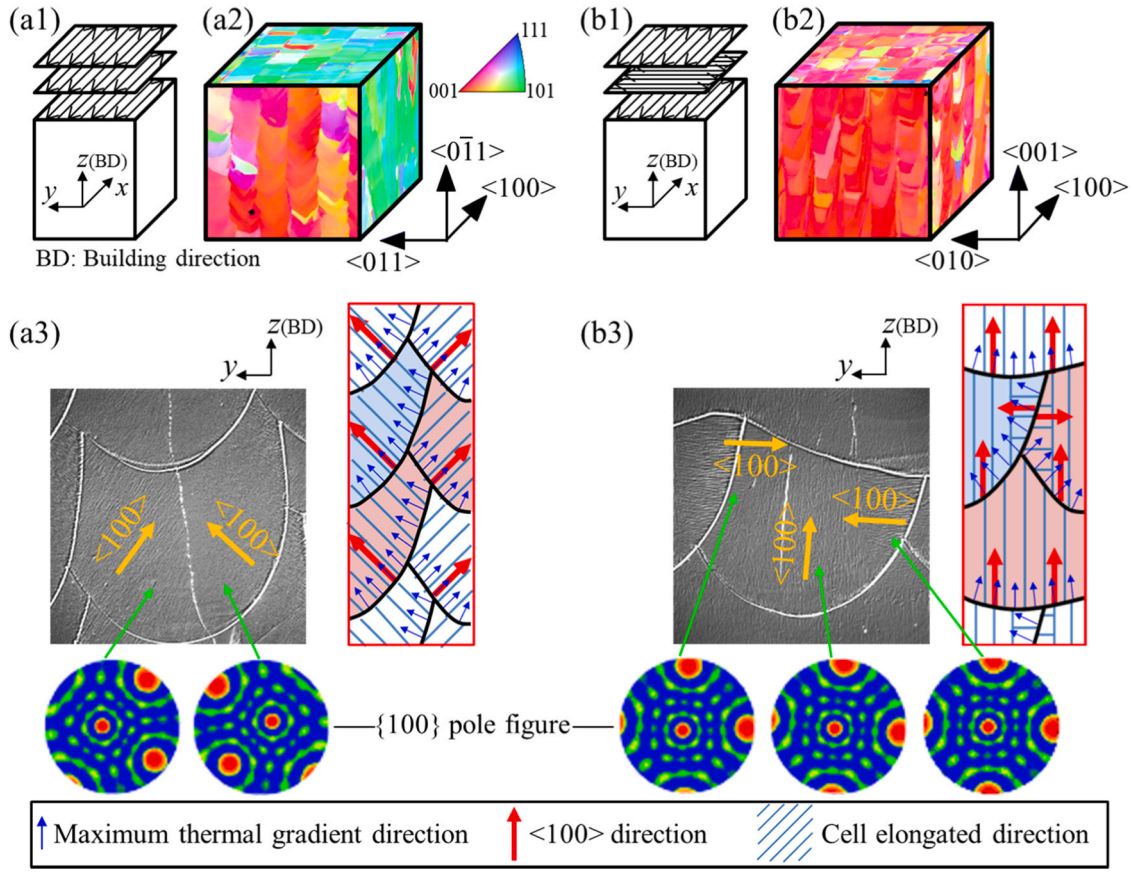

Fig. 1. (a1, b1) Schematic representation of SS_X and SS_XY in the LPBF process and (a2, b2) the developed distinctive crystallographic texture depending on the scanning strategy, referred to as $\{011\}_z\langle 100\rangle_x$ and $\{001\}_z\langle 100\rangle_x$ textures, respectively. (a3, b3) Typical cellular microstructure observed in the *yz*-cross-section of the products and schematics of the mechanism for the texture evolution based on the microstructural observation. This figure was reproduced under the terms of the Creative Commons Attribution 4.0 International license (CC-BY 4.0).
Taken from [14].

2. Experimental procedures

2.1. Experimental design

An ingot with a nominal composition of Ti–15Mo–5Zr–3Al (wt%) was used as the starting material. The powder for LPBF fabrication was developed utilizing Ar gas atomization (Osaka Titanium Technologies Co. Ltd., Japan). The obtained powder was spherical, with a median particle size of 26 μm. Rectangular specimens with a bottom dimension of 5 mm × 5 mm were manufactured using an LPBF apparatus (EOS M 290, EOS, Germany) equipped with a 400 W Yb fiber laser. The fabrication was performed in an Ar atmosphere. Two types of laser-beam scan strategies— SS_X and SS_XY—were used to fabricate the samples.

The crystallographic texture stability during LPBF fabrication was investigated using two methods. The first involved the fabrication of rectangular samples by alternating the scan strategies at a specific height interval during the fabrication process. The scan process parameters, i.e., the laser power, scanning speed, layering thickness, and scan pitch were set to 360 W, 1200 mm/s, 60 μm, and 100 μm, respectively. Under this condition, two alternating scan strategy schemes were attempted: 1) alterative change in SS_X and SS_XY, and 2) alterative change in SS_X and SS_Y. Here, SS_Y denotes that the laser was scanned bidirectionally on the *y*-axis only. The changes in the scan strategy were conducted every 30 layers. A pure Ti plate was used as the starting plate.

The second method used a Ti–15Mo–5Zr–3Al single-crystal with different crystal orientations from the base plate (seed). The Ti–15Mo–5Zr–3Al single-crystal alloy was prepared using the optical floating zone method (SCI-MDH-20020, Canon Machinery, Japan). The crystal growth rate was set at 2.5 mm/h and the single crystal was grown under an Ar atmosphere. The detailed preparation method of the single crystal was described in our previous paper [24]. The crystal orientation was determined using X-ray back-reflection Laue diffraction, and the plates were cut from the obtained single crystal by electron discharge machining. Eight single-crystalline plates with different crystal geometries were prepared for this study. The details of the crystal geometries will be described in Section 3.2 (Fig. 4). Both SS_X and SS_XY strategies were conducted considering the relationship between the crystallographic orientation of the seed and the LPBF-deposited parts.

The microstructures of the prepared samples were examined using optical microscopy (OM; BX60, Olympus, Japan) and field-emission scanning electron microscopy (FE-SEM; JSM-6500, JEOL, Japan). The surface of the sample was mechanically polished using emery papers. Subsequently, final polishing was conducted with colloidal silica. In addition, texture analysis was conducted using an electron backscatter diffraction (EBSD) mounted on the FE-SEM.

2.2. Quantitative evaluation of texture development behavior

To quantitatively analyze the crystallographic texture evolved, the degree of crystal orientation was calculated by the Euler angle measured by SEM-EBSD analysis. In the EBSD analysis, the crystal orientation at each measured pixel along the observed direction was characterized by Euler angles, which are determined as follows:

$$h = \sin\Phi\sin\varphi_2, \quad k = \sin\Phi\cos\varphi_2, \quad l = \cos\Phi \tag{1}$$

Under the specimen coordinate axes (x_s, y_s, and z_s)which are set to the direction perpendicular to the specimen surface and the [100], [010], and [001] directions in the grain are denoted as x_c, y_c, and z_c in the EBSD analysis, the Euler angles of $\varphi_1, \Phi,$ andφ_2 are defined as the angles between the line of intersection of the x_sy_s and x_cy_c planes denoted as N and x_s, the angle between z_s and z_c, and the angle between N and x_c, respectively. Using the <*hkl*> indices measured at each pixel, the degree of crystal orientation of each particular crystal orientation <*uvw*> relative to the observation direction was quantified. First, the angle between the observation direction and <*uvw*> was estimated. For example, in the cubic crystal, there were six and twelve equivalent orientations for <100> and <110>, respectively. Thus, the smallest angle between the observation direction and one of the equivalent orientations of <*uvw*> was defined as $\alpha_{<uvw>}$. Under this definition, the value of $\alpha_{<uvw>}$ is evaluated at each measured pixel and the average value of $\cos^2\alpha_{<uvw>}$ is defined as the degree of crystal orientation for <*uvw*>, denoted as $P_{<uvw>}$. Using the aforementioned definition, the maximum value of $P_{<uvw>}$ is 1, and the closer it is to 1, the stronger the crystal orientation alignment of <*uvw*> along the observation direction. Note, however, that the smaller $P_{<uvw>}$ is not always indicative of a weak texture. For example, the degree of crystal orientation $P_{<100>}$ was smallest when <111> was oriented along the observation direction at all measurement points, thus signifying a single crystal. At this time, $P_{<100>}$ was equal to 1/3. Similarly, the degree of crystal orientation $P_{<110>}$ was the smallest when <100> was oriented along the observation direction at all measurement points when $P_{<110>}$ was 1/2. If the sample is polycrystalline and exhibits a completely random texture, the values of $P_{<100>}$ and $P_{<110>}$ can be calculated as follows:

$$P_{<100>\ in\ random\ polycrystal} = \frac{\int_S \cos^2\alpha_{<100>}dS}{\int_S dS} = \frac{\iint_T z^2\sqrt{1+\left(\frac{\partial z}{\partial x}\right)^2+\left(\frac{\partial z}{\partial y}\right)^2}dxdy}{\iint_T \sqrt{1+\left(\frac{\partial z}{\partial x}\right)^2+\left(\frac{\partial z}{\partial y}\right)^2}dxdy} = \frac{\int_0^{\frac{\pi}{4}}d\theta\int_0^{\frac{1}{\sqrt{\cos^2\theta+1}}} r\sqrt{1-r^2}dr}{\int_0^{\frac{\pi}{4}}d\theta\int_0^{\frac{1}{\sqrt{\cos^2\theta+1}}}\frac{r}{\sqrt{1-r^2}}dr} = \frac{1}{3}+\frac{2}{\sqrt{3}\pi} = 0.7008 \tag{2}$$

$$P_{<110>\ in\ random\ polycrystal} = \frac{\int_S \cos^2\alpha_{<110>}dS}{\int_S dS} = \frac{\iint_T \frac{(x+z)^2}{2}\sqrt{1+\left(\frac{\partial z}{\partial x}\right)^2+\left(\frac{\partial z}{\partial y}\right)^2}dxdy}{\iint_T \sqrt{1+\left(\frac{\partial z}{\partial x}\right)^2+\left(\frac{\partial z}{\partial y}\right)^2}dxdy} = \frac{\int_0^{\frac{\pi}{4}}d\theta\int_0^{\frac{1}{\sqrt{\cos^2\theta+1}}}\frac{r\left(r\cos\theta+\sqrt{1-r^2}\right)^2}{2\sqrt{1-r^2}}dr}{\int_0^{\frac{\pi}{4}}d\theta\int_0^{\frac{1}{\sqrt{\cos^2\theta+1}}}\frac{r}{\sqrt{1-r^2}}dr} = \frac{1}{3}+\frac{\sqrt{3}+1}{\sqrt{3}\pi} = 0.8354 \tag{3}$$

where S is a triangle projected on a spherical surface with a radius of 1 with the [001], [101], and [111] orientations as vertices, and T is the projection of S on the *xy*-plane. z represents a spherical surface (hemisphere) with radius 1 centered on the origin, and $z = \sqrt{1-x^2-y^2}$. Details of the definition of x, y, z are provided in Fig. S1, Supplementary

$$P_{\langle uvw\rangle\ in\ random\ polycrystal} = \frac{1}{3}+\frac{3u^2+\left(2\sqrt{3}-3\right)\left(v^2-w^2\right)+4\left\{uv+\left(1+\sqrt{3}-\sqrt{6}\right)vw+\left(\sqrt{6}-2\right)wu\right\}-1}{\sqrt{3}\pi} \tag{4}$$

Information. Accordingly, a more generalized estimation of $P_{<uvw>}$ in the sample with a completely random texture can be calculated by the following equation:

where, $u \geq v \geq w \geq 0$, and the magnitude of the vector $<uvw>$ is normalized to 1, i.e. $u^2 + v^2 + w^2 = 1$.

3. Results

3.1. Variations in texture when changing the scanning strategy

Fig. 2(a–f) depicts the crystal orientation maps measured in the samples in which the scan strategy was periodically changed. The expected textures formed under the SS_X, SS_XY, and SS_Y used are $\{011\}_z<100>_x$, $\{001\}_z<100>_x$, and $\{011\}_z<01\bar{1}>_x$, respectively. The EBSD analysis was conducted on the *yz*-section perpendicular to the *x*-scanning direction. In Fig. 2, the positions at which the scan strategy was changed are indicated by the horizontal gray lines and arrows. It must be emphasized that the transient behavior of the texture differed depending on the changing scheme of the scan strategy. When focusing on the boundary where the texture was altered, the boundary was almost straight in the transition from SS_X to SS_XY (red dashed lines and arrows in Fig. 2(a–c)). Conversely, the boundary formed irregular waves in the transition from SS_XY to SS_X (blue dashed lines and arrows in Fig. 2 (a–c)). In addition, the area fraction where the $\{011\}_z<100>_x$ and $\{001\}_z<100>_x$ textures were evolved is significantly different, despite, the scan strategy was alternatively changed by the same period (every 30 layers). This can be clearly recognized in Fig. 2(b) and 2(c) in which the area fraction exhibiting the $\{001\}_z<100>_x$ texture (red parts) is considerably wider than that of the $\{011\}_z<100>_x$ texture (green parts).

In the alternative change between SS_X and SS_Y shown in Fig. 2 (d–f), the nature of the evolved texture itself was varied by the alternative change in scan strategy. In the SS_X, the crystal orientation alignment of <100>, <011>, and $<01\bar{1}>$ is expected along the *x*-, *y*-, and *z*-directions, as shown in Fig. 1(a2). Similarly, in the SS_Y, the evolution of the crystal orientation alignment of <110>, <100>, and $<01\bar{1}>$ is expected along the *x*-, *y*-, and *z*-directions. Thus, only the $<01\bar{1}>$ orientation along the *z*-direction (green color in Fig. 2(f)) was expected, however, the unexpected $\{001\}_z<100>_x$ texture (red color in Fig. 2(f)) in which <100> was aligned along the *z*-direction, was evolved in the transient zone between SS_X and SS_Y with a relatively large area fraction.

To discuss the transient behavior of the texture more quantitatively, the degrees of crystal orientation $P_{<100>}$ and $P_{<110>}$ were evaluated along the *z*-direction (BD) in both samples, as shown in Fig. 3. Gray lines and blue/red dashed lines indicate the points at which the scanning strategy was changed and the transient zone was ended, respectively, as similar to Fig. 2. The end point of the transient zone was defined based on the variation in the $P_{<100>}$ and $P_{<110>}$ values; the point where the *P*-value for the expected crystallographic direction under a certain scanning strategy exceeded the values for random orientation. For example, at the change in scan strategy from SS_XY to SS_X ($<110>//z$ is expected), the end point was determined when $P_{<110>}$ along the *z*-direction exceeded the random value (blue dashed lines in Fig. 3(a)); at the change in scan strategy from SS_X to SS_XY ($<100>//z$ is expected), it was determined when $P_{<100>}$ along the *z*-direction exceeded the random value (red dashed lines in Fig. 3(a)). Interestingly, the transient zone width formed in the alternative change between SS_XY and SS_X was not uniform; the width at the SS_XY to SS_X transition was ~790 μm, which was much wider than that at the SS_X to SS_XY transition of ~230 μm.

Considering the alternative change of SS_X and SS_Y shown in Fig. 3 (b), a frequent increase and decrease in $P_{<100>}$ and $P_{<110>}$ were monitored. This is owing to the formation of an unexpected $\{001\}_z<100>_x$ texture despite the expected orientation under SS_X and SS_Y is $<110>//z$. During the alternative change of SS_X and SS_Y, only one pair of SS_XY appears locally at the switching point of scanning strategy. This local SS_XY drastically altered crystallographic orientation into the $\{001\}_z<100>_x$ texture, indicating a high stability of the $\{001\}_z<100>_x$ texture under the SS_XY. Then, the texture showed transition to $<110>//z$ textures.

The expected texture in each scanning strategy was finally formed, however, the transient zone formation behavior until the expected texture appeared differed largely depending on the combination and order of the scanning strategies that were switched. This indicates that the crystallographic texture stability measured by the transient zone formation behavior is influenced by the crystallographic orientation relationship between the pre-solidified substrate and newly deposited parts (expected texture). To systematically understand the texture stability, the "seeding" experiment was performed using single-crystalline substrates and the behavior of transient zone formation or crystallographic orientation inheritance was analyzed.

3.2. Variations in the transient zone width (texture stability) depending on the combination of crystal orientation in single-crystalline substrate and scanning strategy

We used single-crystalline substrates as a seed for LPBF fabrication. The crystal orientation geometry was systematically altered along *x*-, *y*-, and *z*-directions as schematically described in Fig. 4. Eight different controlled crystal orientations were selected as a seed for fabrication using the SS_X and SS_XY. In the fabrication using the SS_X, in addition to the single-crystalline substrate in which the orientation correlated entirely with that in the $\{011\}_z<100>_x$ texture (Fig. 4(a1)), three other single-crystalline substrates in which only one orientation (*x*-, *y*-, or *z*-orientation) corresponded to that in the $\{011\}_z<100>_x$ texture (Fig. 4 (a2–a4)) were prepared. Hereinafter, they are referred to as *xyz*-, *x*-, *y*-, and *z*-common SS_X substrates, respectively. Similarly, the *xyz*-, *x*-, *z*-common single-crystalline substrates were prepared for SS_XY with respect to the $\{001\}_z<100>_x$ texture (Fig. 4(b1–b3)). In addition, the single-crystalline substrate in which any of the three *x*-, *y*-, and *z*-orientations did not coincide with those in the $\{001\}_z<100>_x$ texture (Fig. 4(b4)) was also prepared for the SS_XY (hereinafter the uncommon SS_XY substrate).

Figs. 5 and 6 depict the crystal orientation maps showing the variations in texture evolution depending on the crystal orientation in the single-crystalline seed for the SS_X and SS_XY products, respectively. In the figures, the corresponding variations in $P_{<100>}$, $P_{<110>}$, $P_{<111>}$, and $P_{<112>}$ are also displayed below the crystal orientation maps. The graphs on *P*-value in the upper row indicate the variation in initial (single-crystalline seed) orientation, and those in the lower row indicate the variation in the expected orientation to be formed under each scanning strategy. Here, the time point at which the $P_{<100>}$ and $P_{<110>}$ satisfied all of the following states was defined as the end point of the transient zone: for SS_X, $P_{<100>}$ along the *x*-direction and $P_{<110>}$ along the *y*- and *z*-directions exceeded the values for random orientation; for SS_XY, $P_{<100>}$ along the *x*-, *y*-, and *z*-directions exceeded the values for random orientation.

In the *xyz*-common SS_X sample, the evolution of the $\{011\}_z<100>_x$ texture was confirmed without the formation of a transient zone, as shown in Fig. 5(a). Similarly, the $\{001\}_z<100>_x$ texture was evolved in the *xyz*-common SS_XY sample (Fig. 6(a)). In these cases, the *P*-values in all directions remained higher than those in randomly oriented polycrystalline. The crystal orientations in the single-crystalline substrate were inherited into the newly deposited portion, indicating successful "seeding" under LPBF. However, the formation of the transient zone of the texture was observed in all the other cases. Importantly, the width of the transient zone of the texture was considerably different depending on the crystal geometry of the single-crystalline substrate and the scan strategy, as hypothesized in the previous section. Table 1 summarizes the measured transient zone width.

The seeding experiment using single-crystalline substrates derived

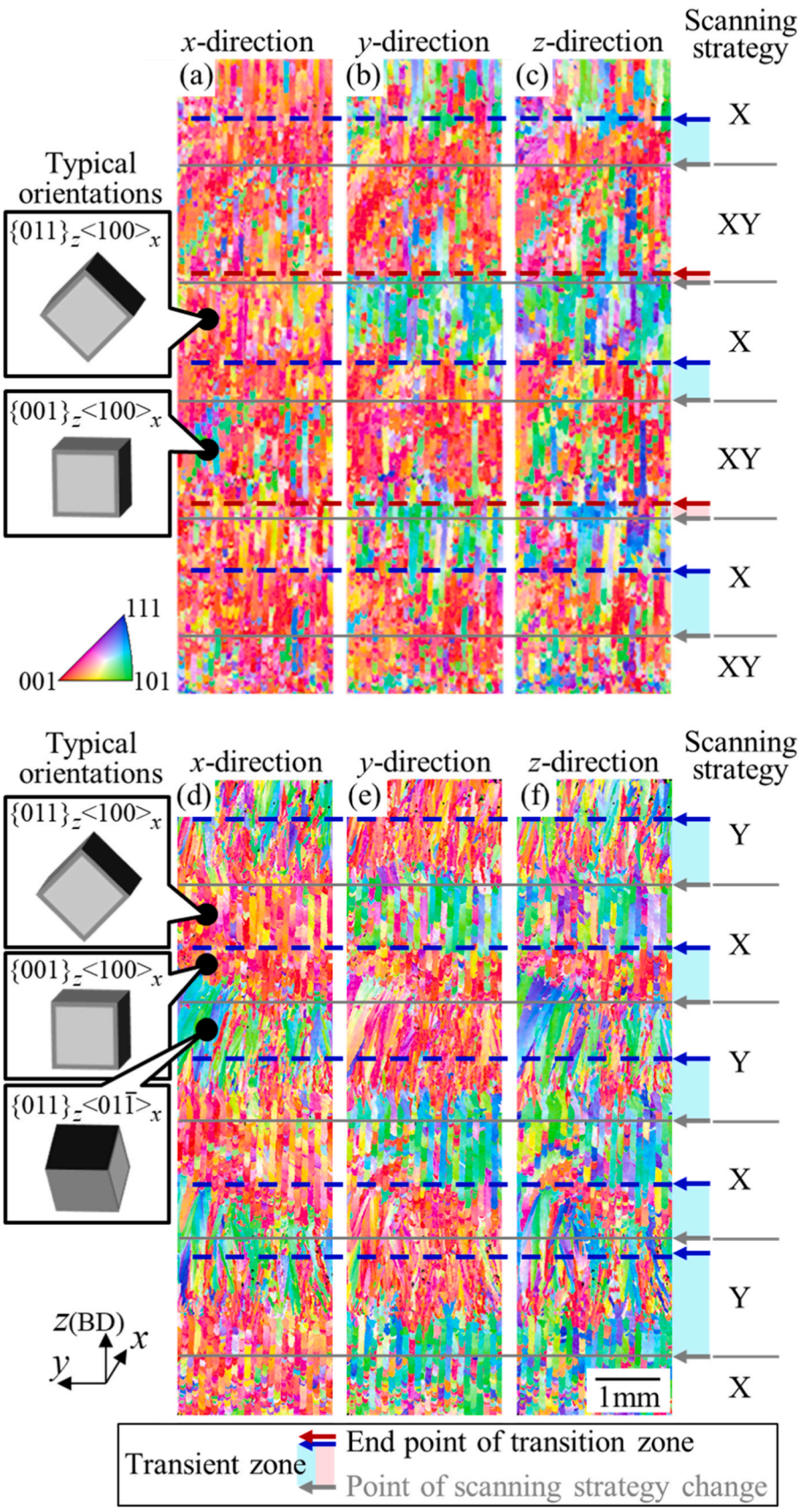

Fig. 2. Crystal orientation maps showing the variation in texture by changing the scanning strategy during the fabrication of the samples. (a–c) Alternative change in the SS_X and SS_XY and (d–f) alternative change in the SS_X and SS_Y. The observation was conducted on the *yz*-plane and the crystal orientation colors indicated those along the (a, d) *x*-, (b, e) *y*-, and (c, f) *z*-directions, respectively. The positions where the scanning strategy was changed are indicated by horizontal gray lines, and the positions where the resultant change in texture occurred are indicated by blue and red dashed lines.

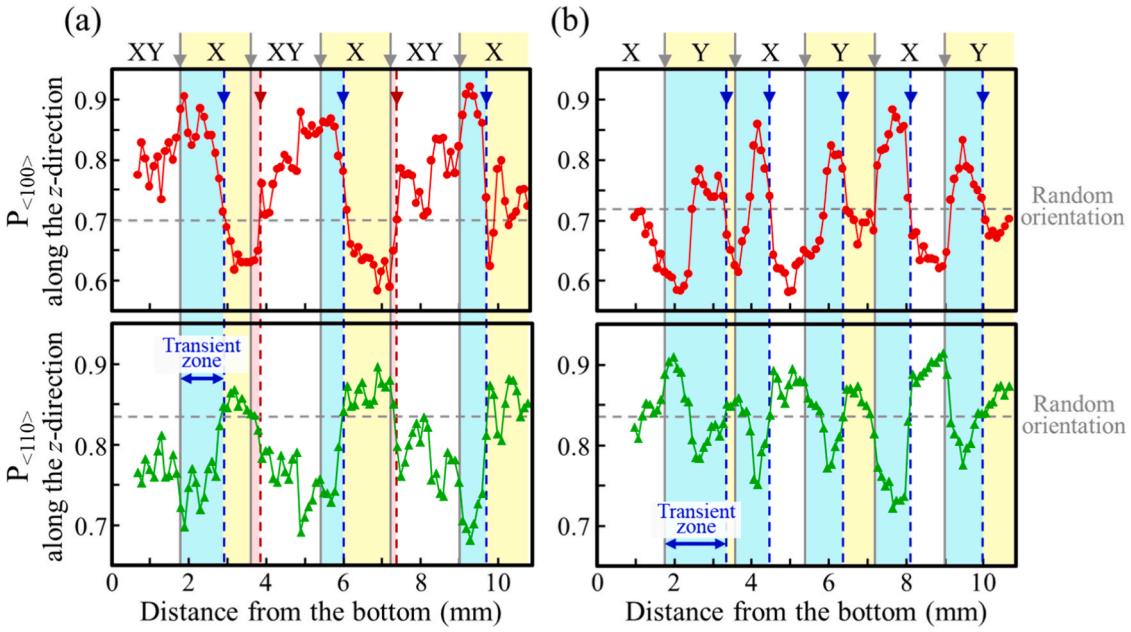

Fig. 3. Variation in the degree of crystal orientation alignment $P_{<100>}$ and $P_{<110>}$ along the *z*-direction in the following samples: (a) SS_X/SS_XY and (b) SS_X/SS_Y. The positions where the scanning strategy was changed are indicated by vertical gray lines, and the positions where the resultant change in texture occurred are indicated by blue and red dashed lines.

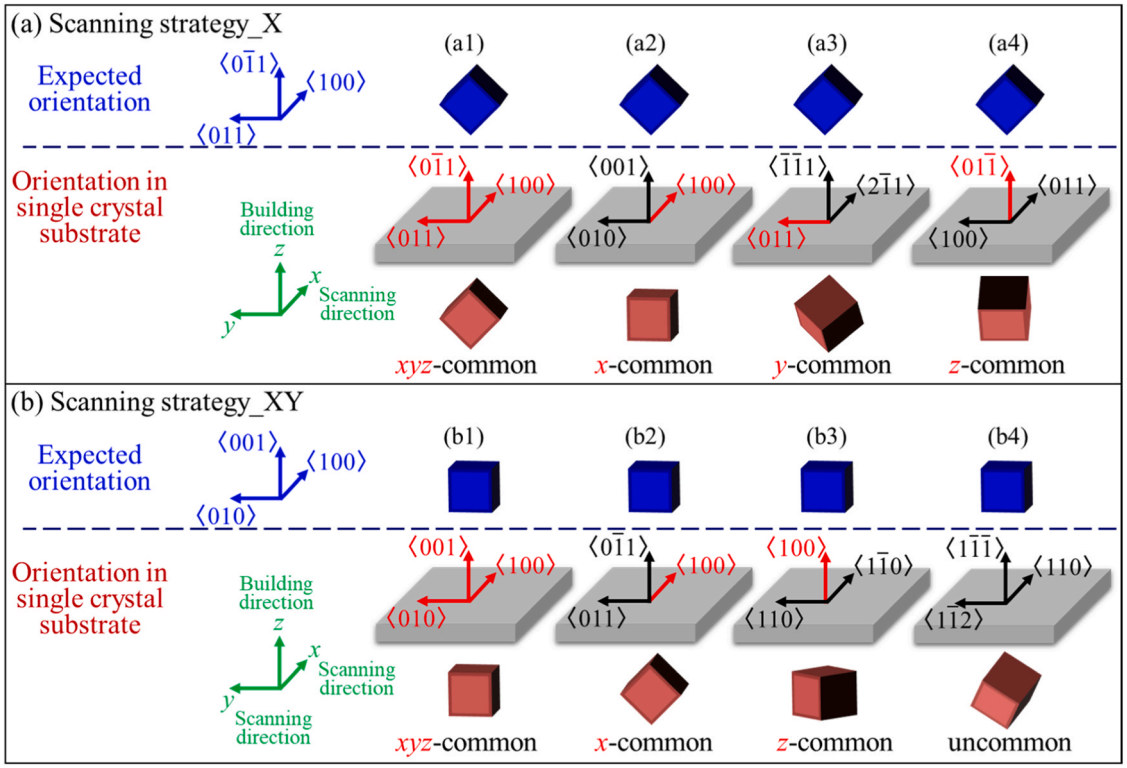

Fig. 4. Eight different geometries of the single crystal used as a base plate in the experiment to clarify the variation in the epitaxial growth behavior of the columnar cells during the LPBF process.

the following two important findings. 1) The transient zone width is wider in the *x*-, and *y*-common samples than those in the *z*-common samples, in both the SS_X and SS_XY fabrications. Comparing between the *x*-, and *y*-common samples, transient zone width is wider in the *x*-common sample. 2) In the case where the laser scanning directions (*x*-direction in SS_X and *x*- and *y*-directions in SS_XY) were parallel to the <100> direction in the substrate, the crystal orientation tended to be inherited over a certain distance, otherwise the crystal orientation switched rapidly, such that the <100> orientation was parallel to the scanning direction(s). This conclusion was quantitatively confirmed by demonstrating the variation in the transient zone width as a function of the deviation angle of the crystal orientation along the BD (Fig. 7(a)) or

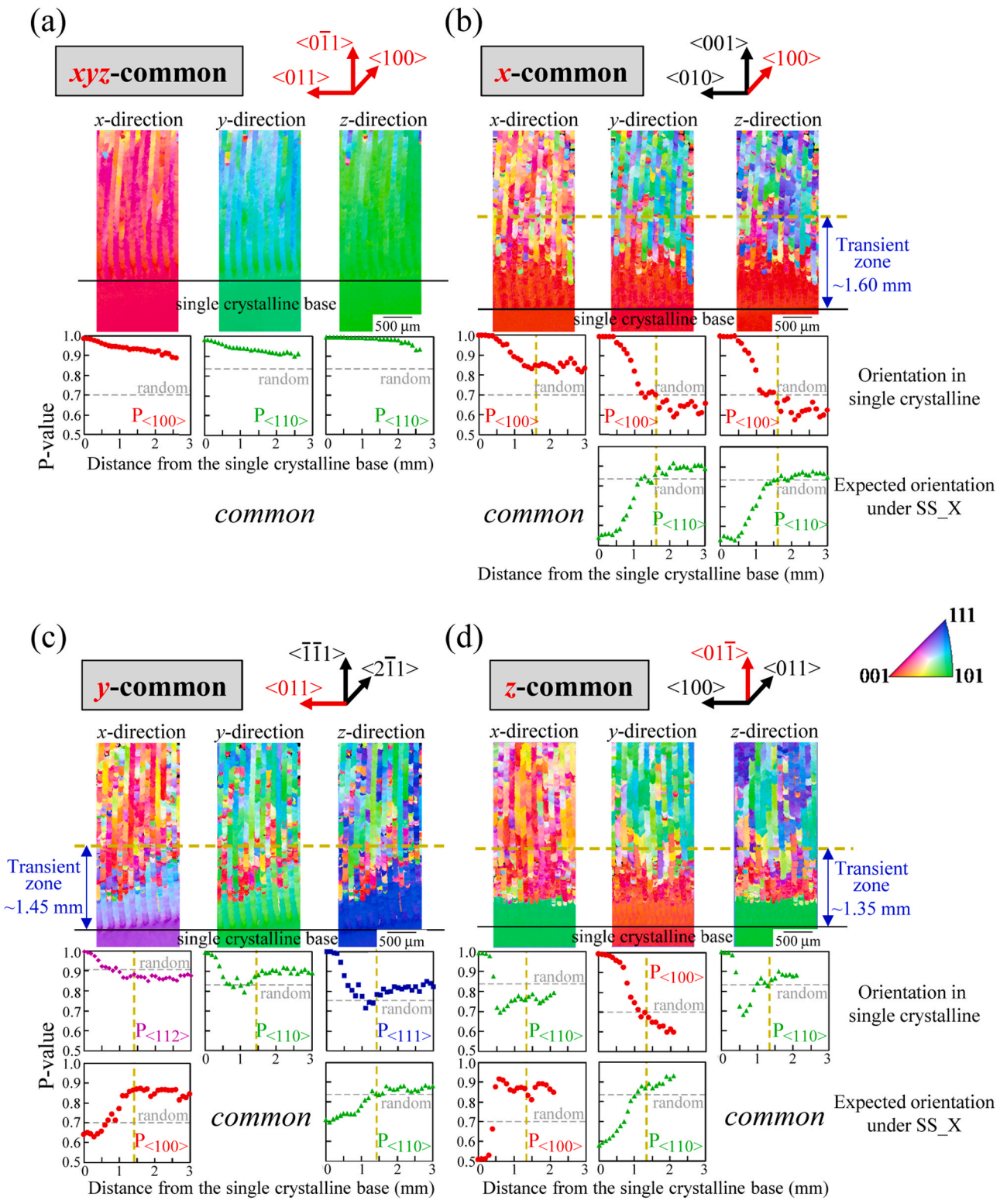

Fig. 5. Crystal orientation maps showing the variation in the developing texture depending on the geometry of the crystal orientation of the starting plate in the fabrication with SS_X. The starting plates are (a) *xyz*-common, (b) *x*-common, (c) *y*-common, and (d) *z*-common single-crystalline plates, respectively. The microstructure observation was conducted on the *yz*-section, and the crystal orientation along the *x*-, *y*-, and *z*-directions are displayed, as indicated in the figure. Below the maps, the corresponding variations in $P_{<100>}$, $P_{<110>}$, $P_{<111>}$ and/or $P_{<112>}$ are also displayed.

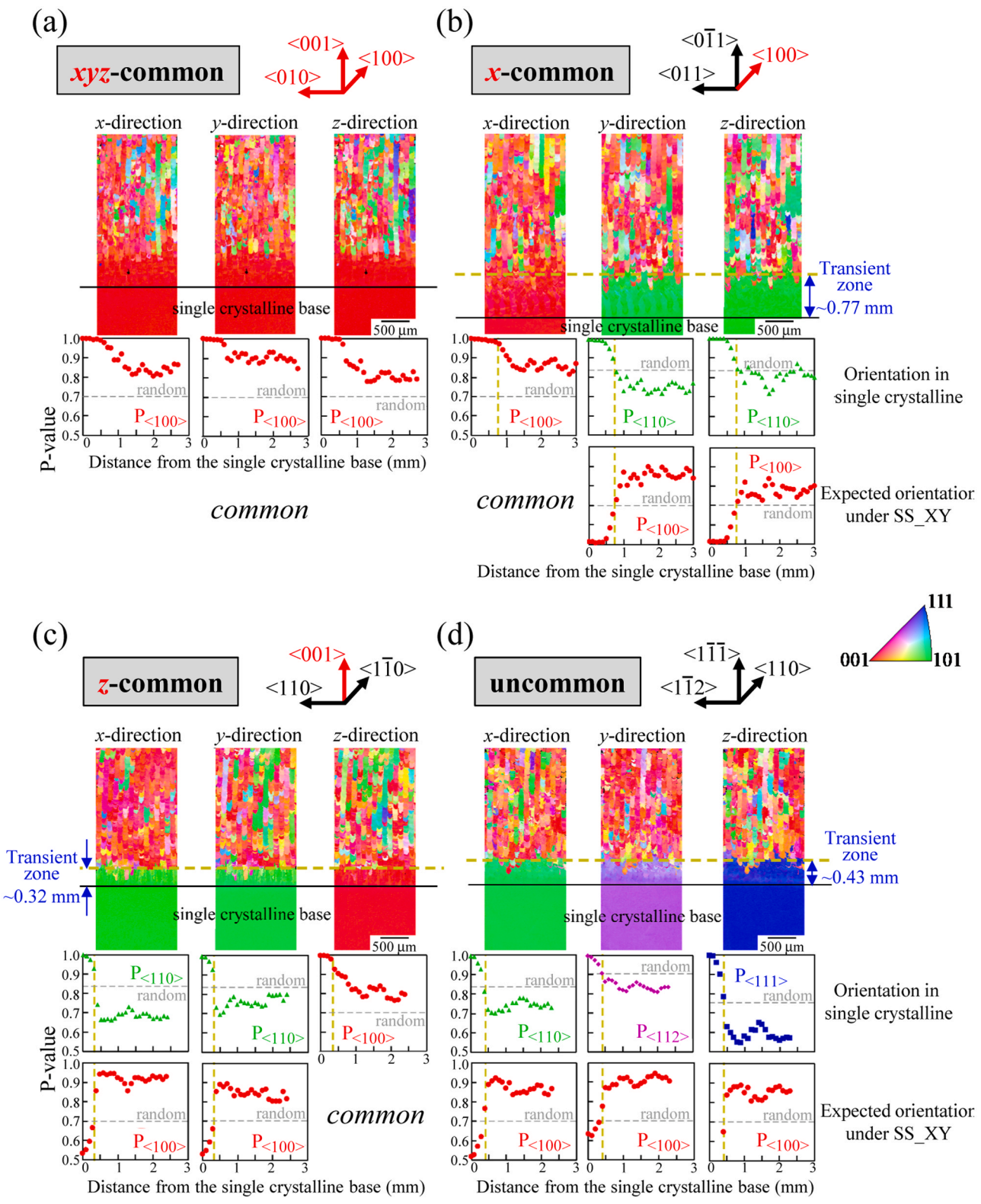

Fig. 6. Crystal orientation maps showing the variation in the developing texture depending on the geometry of the crystal orientation of the starting plate in the fabrication with SS_XY. The starting plates are (a) *xyz*-common, (b) *x*-common, (c) *z*-common, and (d) uncommon single-crystalline plates, respectively. The microstructure observation was conducted on the *yz*-section, and the crystal orientation along *x*-, *y*-, and *z*-directions are displayed, as indicated in the figure. Below the maps, the corresponding variations in $P_{<100>}$, $P_{<110>}$, $P_{<111>}$, and/or $P_{<112>}$ are also displayed.

Table 1
The difference in the width of the transient zone of the texture measured in Figs. 5 and 6, which is varied depending on the geometry of the crystal orientation of the starting plate and scanning strategy.

SS_X	***xyz*-common**	***x*-common**	***y*-common**	***z*-common**
Difference in angle along *z*-direction (BD) (deg.)	0	45	35.3	0
Difference in angle along scanning direction (deg.)	0	0	35.3	45
Transient zone width (mm)	–	1.60	1.45	1.35
SS_XY	***xyz*-common**	***x*-common**	***z*-common**	**Uncommon**
Difference in angle along *z*-direction (BD) (deg.)	0	45	0	55
Difference in angle along scanning direction (deg.)	0	0	45	35
Transient zone width (mm)	–	0.77	0.32	0.43

the laser scanning direction(s) (Fig. 7(b)) between the single-crystalline substrate and the expected $\{011\}_z\langle 100\rangle_x$ or $\{001\}_z\langle 100\rangle_x$ textures. In the case of SS_XY, since there are equivalent two scanning directions, the smaller values of the two are plotted as the deviation angles for the scanning direction. The width of the transient zone decreased as the deviation angle increased with respect to the scanning direction (Fig. 7(b)). Conversely, the difference in the deviation angle along the BD exhibited no correlation with the width of the transient zone (Fig. 7(a)).

4. Discussion

4.1. Formation of the transient zone and the stability of the crystallographic texture in LPBF

In both the SS_X and SS_XY fabrications, the transient zone width is wider when the laser scanning direction is parallel to the <100> orientation in the substrate as typically shown in Figs. 5(b) and 6(b). In this case, the crystal orientation tended to be inherited over a relatively longer distance and subsequently transitions to the expected texture for the scanning strategy selected. When the laser scanning direction deviates from <100> in the substrate, the crystal orientation switched rapidly, so that <100> orients in the scanning direction(s) (Figs. 5(c and d) and 6(c and d)). These findings strongly demonstrate that the crystallographic <100> orientation along the "scanning direction" stabilized within a relatively short time and lead the texture formation in the LPBF process. The stability of the texture in which <100> was parallel to the scanning direction was significantly higher than that of other textures irrespective to the scanning strategy (SS_X or SS_XY). This insight is completely different from the frequently seen explanation that the crystal orientation along the *z*-direction (BD) determines the texture evolution in LPBF [25–27]. Actually, the initial crystal orientation along the building direction has less effect on the texture stability in the case of LPBF process. The stability of the crystallographic orientation is determined by the orientation relationship (difference) between the scanning direction and the <100> direction in the pre-solidified underneath portion that acts as the substrate.

The transient zone width was narrower in the SS_XY samples than in the SS_X sample. In the case of SS_XY, the two-dimensional cellular growth alternatively occurs on *yz*- (for X-scan) and *xz*-planes (for Y-scan). As a result, the <100> shows strong tendency to orient in the normal directions on the two planes (i.e., the *x*- and *y*-scanning directions), which simultaneously fix the alignment of the remaining <001> to the *z*-direction (BD). As a result, the $\{001\}_z\langle 100\rangle_x$ texture in SS_XY evolves more rapidly than the $\{011\}_z\langle 100\rangle_x$ texture in SS_X.

The high stability of the $\{001\}_z\langle 100\rangle_x$ texture under the SS_XY would largely influence the transient zone formation in the fabrication with the alternative change of SS_X and SS_Y (Figs. 2(d–f) and 3(b)). The alternative change of SS_X and SS_Y was well reproduced by the seeding experiment using the combination of SS_X and single-crystalline substrate with *z*-common orientation (Fig. 5(d)). The $\{001\}_z\langle 100\rangle_x$ texture that is unexpected for the SS_X and SS_Y, while expected for SS_XY was evolved following to the switch of the scanning strategy. In the alternative change of SS_X and SS_Y, SS_XY is locally established which is made up of only two layers at the switching point of scanning strategy. Even this locally established SS_XY domain induced unexpected $\{001\}_z\langle 100\rangle_x$ texture owing to its high stability.

4.2. Evolution mechanism of the crystallographic texture depending on the scanning strategy, considering the competitive and epitaxial crystal growth in the melt pool

The <100> orientation in the substrate being parallel to the laser scanning direction(s) was demonstrated to be important for the stability of crystallographic texture evolution during LPBF. In order to understand the crystallographic stability not only in the laser scanning direction but also in the other directions that are typically considered in

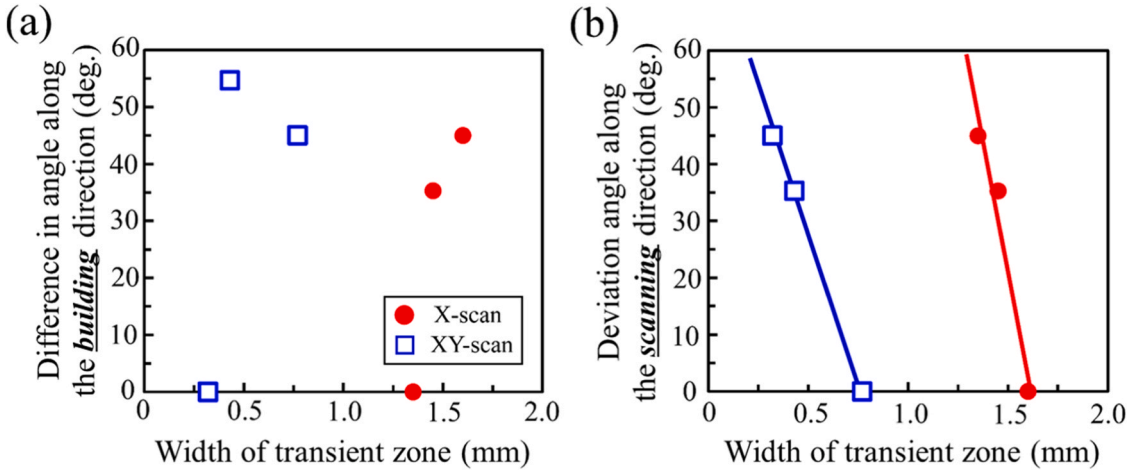

Fig. 7. Relation between the width of the transient area and the difference in the crystal orientation angles in the base single crystal and the developed $\{011\}_z\langle 100\rangle_x$ or $\{001\}_z\langle 100\rangle_x$ texture in SS_X or SS_XY, respectively, focused along the (a) building direction (BD), and (b) scanning direction.

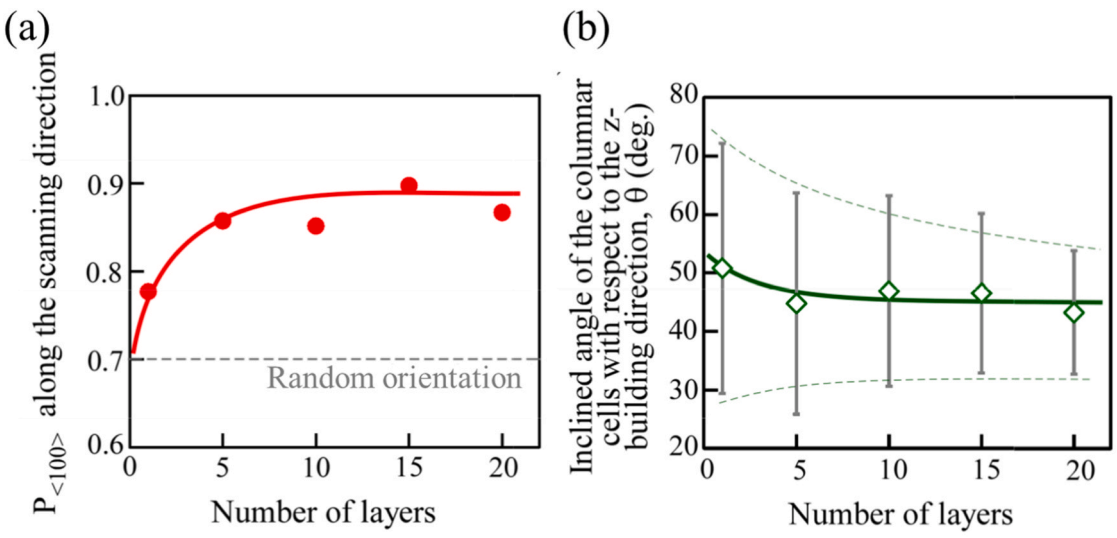

Fig. 8. (a) Variations in $P_{<100>}$ and (b) the inclined angle of the elongation direction of the columnar cells with respect to the z-building direction (θ) with the number of stacking layer, measured on the yz-plane of the sample fabricated by SS_X. The fabrication was conducted on a pure α-Ti plate with the hcp structure to minimize the influence of the epitaxial growth impacted from the starting plate.

the LPBF process, the texture transition behavior was analyzed at the initial stage of the deposition. The LPBF fabrication was performed with a simple SS_X. The variations in $P_{<100>}$ along the x-scanning direction (Fig. 8(a)) and the inclined angle (θ) of the elongation direction of the <100>-oriented columnar cells with respect to the BD (Fig. 8(b)), were measured as a function of the number of stacking layers. The yz-cross-section that is perpendicular to the x-scanning direction was used to appropriately analyze the cellular angles. The fabrication was conducted on a pure α-Ti plate with the hexagonal close-packed (hcp) structure to avoid the influence of the epitaxial growth from the base plate.

The variation in $P_{<100>}$ shown in Fig. 8(a) demonstrated that the <100> orientation along the x-scanning direction rapidly stabilized within the first few layers of deposition. On the other hand, the inclined angle of the columnar cells exhibited a wide distribution between ~30° and ~70° at the initial stage, and gradually converged in the ±45° direction as the number of stacking layers increased. Consequently, the $\{011\}_z<100>_x$ texture stabilized and epitaxial growth occurred, as reported in the previous paper [14]. These results strongly indicated that at the initial stage of deposition, the crystal orientation in the scanning direction was first stabilized, then the orientation (<100>-oriented cell growth direction) within the melt pool cross-section was secondary determined. The inclined angle of the columnar cells of ±45° is considered to be advantageous for the reduction of interfacial energy at the center of the melt pool, where the solidification front of the right and left sides encounters. Therefore, the orientation perpendicular to the x-direction is adjusted so that the crystallographic misorientation in the right and left sides of the melt pool reduces, leading to the ±45° cells from BD and <110>//z orientation.

In the SS_XY, in contrast, the fact that <100> orientation in the scanning direction is important as similar to the previous situation would leads to competition for crystal orientations. When the scanning direction was changed from X-scan (the texture where <100>//x-direction and <011>//y-direction are stable) to Y-scan (the texture where <100>//y-direction and <011>//x-direction are stable), the <011> orientation in the pre-solidified layer formed by X-scan and <100>-orientation generated by Y-scan competed with each other in the y-direction. The crystal orientation was determined through the competition of crystal growth. Since <100> grows faster [23], <100> could remain in the y-direction, whereas <011> was eliminated. In SS_XY, the competition also occurred in the x-direction, resulting in the texture in which <100> oriented in x- and y-directions, and resultantly the z-directions as well.

4.3. Application of the crystallographic texture control

By exploiting the feature that metal AM enables the scan strategy to be altered in a site-selective manner within a part, a promising methodology for enhancing the functionality of structural parts is to three-dimensionally collocate elements with different crystallographic textures in order to tailor the mechanical properties as desired. To achieve this, it is necessary to superimpose an element with different crystallographic orientations on the underneath layer. Such a strategy must be of great help to functionalization of biomedical devices such as orthopedic and/or dental implants because the implant devices should adopt to the complicated stress applied in vivo with simultaneously suppressing a stress shielding [28] on surrounding bone tissues. It is desired to tailor mechanical properties e.g., Young's modulus depending on the location in the part and the direction. The findings regarding the texture stability obtained in this study are beneficial to achieve the series stacking of elements with different textures in the vertical (building) direction. By increasing the strength of the texture formed, it is expected that the transient zone width can be predicted uniformly. Strengthening the texture is one of the challenges in future research. In addition, the investigation of the texture stability in other alloy systems is needed to utilize this strategy in a wide range of industries.

5. Conclusions

In this study, the stability of the crystallographic texture during LPBF fabrication was investigated. The following conclusions were drawn:

(1) In SS_X in which the $\{011\}_z<100>_x$ texture formed, <100> was first stabilized in the laser scanning (x-) direction. Within the yz-plane in the melt pool cross-section, the <100>-elongated cell gradually aligned in the direction of ±45° from the BD, resulting in reduced interface energy in the melt pool center.
(2) In SS_XY in which the $\{001\}_z<100>_x$ texture formed, <100> and <011> competed to grow in the laser scanning direction. Because of the more rapid growth rate in the <100> direction, <100> remained in both the scanning directions (x- and y-directions), and thus the remaining <001> was fixed in the z-direction.

(3) The stability of the crystallographic texture varied depending on the orientation in the substrate. In the case where the laser scanning direction was parallel to the <100> direction in the substrate, the crystal orientation was likely to be inherited. Interestingly, however, the crystallographic orientation along the *z*-direction (BD) in the substrate did not impact the stability of the texture. Thus, the <100> orientation in the scanning direction determined the texture formation, irrespective of SS_X or SS_XY.
(4) Using a single crystal as a seeding substrate, it was possible to produce a single crystalline region under the LPBF process. The crystallographic orientation in the seed must be selected by considering the stability of the texture depending on the scanning strategy.

The formation of the crystallographic texture during LPBF fabrication is largely determined by the relationship between the laser scanning direction(s) and crystal orientation in the underneath solidified layer. This is peculiar to layer-by-layer fabrication, which is impacted by both the influence of the underneath layer and the solidification behavior in the melt pool itself. It is expected that functional devices, such as biomedical implants, with a configuration of differently textured portions will be created by carefully considering the stability of the texture.

CRediT authorship contribution statement

Takuya Ishimoto: Methodology, Validation, Investigation, Data curation, Writing - review & editing. **Koji Hagihara**: Investigation, Data curation, Writing - original draft, **Kenta Hisamoto**: Investigation, Data curation, Visualization, **Takayoshi Nakano**: Conceptualization, Writing - review & editing, Supervision, Project administration, Funding acquisition.

Declaration of Competing Interest

The authors declare that they have no known competing financial interests or personal relationships that could have appeared to influence the work reported in this paper.

Acknowledgement

Funding: This work was supported by Grants-in-Aid for Scientific Research (JP18H05254 and JP19H00827) from the Japan Society for the Promotion of Science (JSPS). This work was also partly supported by the Cross-Ministerial Strategic Innovation Promotion Program (SIP), Materials Integration for Revolutionary Design System of Structural Materials, Domain C1: “Development of Additive Manufacturing Process for Ni-based Alloy” from the Japan Science and Technology Agency (JST).

Appendix A. Supporting information

Supplementary data associated with this article can be found in the online version at doi:10.1016/j.addma.2021.102004.

References

[1] J. Plocher, A. Panesar, Review on design and structural optimisation in additive manufacturing: towards next-generation lightweight structures, Mater. Des. 183 (2019), 108164, https://doi.org/10.1016/j.matdes.2019.108164.
[2] L. Bai, C. Gong, X. Chen, Y. Sun, J. Zhang, L. Cai, S. Zhu, S.Q. Xie, Additive manufacturing of customized metallic orthopedic implants: materials, structures, and surface modifications, Metals 9 (2019) 1004, https://doi.org/10.3390/met9091004.
[3] P. Wang, X. Li, Y. Jiang, M.L.S. Nai, J. Ding, J. Wei, Electron beam melted heterogeneously porous microlattices for metallic bone applications: design and investigations of boundary and edge effects, Addit. Manuf. 36 (2020), 101556, https://doi.org/10.1016/j.addma.2020.101566.
[4] S.F. Shirazi, S. Gharehkhani, M. Mehrali, H. Yarmand, H.S. Metselaar, N. Adib Kadri, T.A. Osman, A review on powder-based additive manufacturing for tissue engineering: selective laser sintering and inkjet 3D printing, Sci. Technol. Adv. Mater. 16 (2015), 033502, https://doi.org/10.1088/1468-6996/16/3/033502.
[5] M. Orme, I. Madera, M. Gschweitl, M. Ferrari, Topology optimization for additive manufacturing as an enabler for light weight flight hardware, Designs 2 (2018) 51, https://doi.org/10.3390/designs2040051.
[6] P. Wang, J. Song, M.L.S. Nai, J. Wei, Experimental analysis of additively manufactured component and design guidelines for lightweight structures: a case study using electron beam melting, Addit. Manuf. 33 (2020), 101088, https://doi.org/10.1016/j.addma.2020.101088.
[7] T. Ishimoto, S. Wu, Y. Ito, S.-H. Sun, H. Amano, T. Nakano, Crystallographic orientation control of 316L austenitic stainless steel via selective laser melting, ISIJ Int. 60 (2020) 1758–1764, https://doi.org/10.2355/isijinternational.ISIJINT-2019-744.
[8] M.S. Pham, B. Dovgyy, P.A. Hooper, C.M. Gourlay, A. Piglione, The role of side-branching in microstructure development in laser powder-bed fusion, Nat. Commun. 11 (2020) 749, https://doi.org/10.1038/s41467-020-14453-3.
[9] S.-H. Sun, T. Ishimoto, K. Hagihara, Y. Tsutsumi, T. Hanawa, T. Nakano, Excellent mechanical and corrosion properties of austenitic stainless steel with a unique crystallographic lamellar microstructure via selective laser melting, Scr. Mater. 159 (2019) 89–93, https://doi.org/10.1016/j.scriptamat.2018.09.017.
[10] O. Andreau, I. Koutiri, P. Peyre, J.-D. Penot, N. Saintier, E. Pessard, T. De Terris, C. Dupuy, T. Baudin, Texture control of 316L parts by modulation of the melt pool morphology in selective laser melting, J. Mater. Process. Technol. 264 (2019) 21–31, https://doi.org/10.1016/j.jmatprotec.2018.08.049.
[11] H.Y. Wan, Z.J. Zhou, C.P. Li, G.F. Chen, G.P. Zhang, Effect of scanning strategy on grain structure and crystallographic texture of Inconel 718 processed by selective laser melting, J. Mater. Sci. Technol. 34 (2018) 1799–1804, https://doi.org/10.1016/j.jmst.2018.02.002.
[12] S.-H. Sun, K. Hagihara, T. Nakano, Effect of scanning strategy on texture formation in Ni-25 at%Mo alloys fabricated by selective laser melting, Mater. Des. 140 (2018) 307–316, https://doi.org/10.1016/j.matdes.2017.11.060.
[13] K. Hagihara, T. Nakano, M. Suzuki, T. Ishimoto, Suyalatu, S.-H. Sun, Successful additive manufacturing of $MoSi_2$ including crystallographic texture and shape control, J. Alloy. Compd. 696 (2017) 67–72, https://doi.org/10.1016/j.jallcom.2016.11.191.
[14] T. Ishimoto, K. Hagihara, K. Hisamoto, S.-H. Sun, T. Nakano, Crystallographic texture control of beta-type Ti-15Mo-5Zr-3Al alloy by selective laser melting for the development of novel implants with a biocompatible low Young’s modulus, Scr. Mater. 132 (2017) 34–38, https://doi.org/10.1016/j.scriptamat.2016.12.038.
[15] X. Luan, H. Qin, F. Liu, Z. Dai, Y. Yi, Q. Li, The mechanical properties and elastic anisotropies of cubic Ni_3Al from first principles calculations, Crystals 8 (2018) 307, https://doi.org/10.3390/cryst8080307.
[16] M. Tane, S. Akita, T. Nakano, K. Hagihara, Y. Umakoshi, M. Niinomi, H. Nakajima, Peculiar elastic behavior of Ti–Nb–Ta–Zr single crystals, Acta Mater. 56 (2008) 2856–2863, https://doi.org/10.1016/j.actamat.2008.02.017.
[17] W. Kaita, K. Hagihara, L.A. Rocha, T. Nakano, Plastic deformation mechanisms of biomedical Co–Cr–Mo alloy single crystals with hexagonal close-packed structure, Scr. Mater. 142 (2018) 111–115, https://doi.org/10.1016/j.scriptamat.2017.08.016.
[18] T.P. Gabb, J. Gayda, R.V. Miner, Orientation and temperature dependence of some mechanical properties of the single-crystal nickel-base superalloy René N4: Part II. Low cycle fatigue behavior, Metall. Trans. A 17 (1986) 497–505, https://doi.org/10.1007/BF02643956.
[19] V. Sass, U. Glatzel, M. Feller-Kniepmeier, Anisotropic creep properties of the nickel-base superalloy CMSX-4, Acta Mater. 44 (1996) 1967–1977, https://doi.org/10.1016/1359-6454(95)00315-0.
[20] N. Nadammal, S. Cabeza, T. Mishurova, T. Thiede, A. Kromm, C. Seyfert, L. Farahbod, C. Haberland, J.A. Schneider, P.D. Portella, G. Bruno, Effect of hatch length on the development of microstructure, texture and residual stresses in selective laser melted superalloy Inconel 718, Mater. Des. 134 (2017) 139–150, https://doi.org/10.1016/j.matdes.2017.08.049.
[21] O. Gokcekaya, N. Hayashi, T. Ishimoto, K. Ueda, T. Narushima, T. Nakano, Crystallographic orientation control of pure chromium via laser powder-bed fusion and improved high temperature oxidation resistance, Addit. Manuf. 36 (2020), 101624, https://doi.org/10.1016/j.addma.2020.101624.
[22] F. Geiger, K. Kunze, T. Etter, Tailoring the texture of IN738LC processed by selective laser melting (SLM) by specific scanning strategies, Mater. Sci. Eng. A 661 (2016) 240–246, https://doi.org/10.1016/j.msea.2016.03.036.
[23] R.W. Messler, Principles of Welding, Wiley, New York, 2008.
[24] S.-H. Lee, M. Todai, M. Tane, K. Hagihara, H. Nakajima, T. Nakano, Biocompatible low Young’s modulus achieved by strong crystallographic elastic anisotropy in Ti-15Mo-5Zr-3Al alloy single crystal, J. Mech. Behav. Biomed. Mater. 14 (2012) 48–54, https://doi.org/10.1016/j.jmbbm.2012.05.005.
[25] L. Thijs, S. Montero, M.L. Sistiaga, R. Wauthle, Q. Xie, J.P. Kruth, J. van Humbeeck, Strong morphological and crystallographic texture and resulting yield strength anisotropy in selective laser melted tantalum, Acta Mater. 61 (2013) 4657–4668, https://doi.org/10.1016/j.actamat.2013.04.036.
[26] L.N. Carter, C. Martin, P.J. Withers, M.M. Attallah, The influence of the laser scan strategy on grain structure and cracking behaviour in SLM powder-bed fabricated nickel superalloy, J. Alloy. Compd. 615 (2014) 338–347, https://doi.org/10.1016/j.jallcom.2014.06.172.
[27] B.E. Carroll, T.A. Palmer, A.M. Besse, Anisotropic tensile behavior of Ti-6Al-4V components fabricated with directed energy deposition additive manufacturing, Acta Mater. 87 (2015) 309–320, https://doi.org/10.1016/j.actamat.2014.12.054.
[28] R. Huiskes, H. Weinans, B. Van Rietbergen, The relationship between stress shielding and bone resorption around total hip stems and the effects of flexible materials, Clin. Orthop. Relat. Res. 274 (1992) 124–134, https://doi.org/10.1097/00003086-199201000-00014.